



Physical oceanographic conditions and a sensitivity study on meltwater runoff in a West Greenland fjord: Kangerlussuaq

Monteban, Dennis; Pedersen, Jens Olaf Pepke; Nielsen, Morten Holtegaard

Published in:
Oceanologia

Link to article, DOI:
[10.1016/j.oceano.2020.06.001](https://doi.org/10.1016/j.oceano.2020.06.001)

Publication date:
2020

Document Version
Publisher's PDF, also known as Version of record

[Link back to DTU Orbit](#)

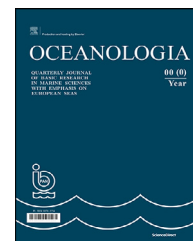
Citation (APA):
Monteban, D., Pedersen, J. O. P., & Nielsen, M. H. (2020). Physical oceanographic conditions and a sensitivity study on meltwater runoff in a West Greenland fjord: Kangerlussuaq. *Oceanologia*, 62(4), 460-477. <https://doi.org/10.1016/j.oceano.2020.06.001>

General rights

Copyright and moral rights for the publications made accessible in the public portal are retained by the authors and/or other copyright owners and it is a condition of accessing publications that users recognise and abide by the legal requirements associated with these rights.

- Users may download and print one copy of any publication from the public portal for the purpose of private study or research.
- You may not further distribute the material or use it for any profit-making activity or commercial gain
- You may freely distribute the URL identifying the publication in the public portal

If you believe that this document breaches copyright please contact us providing details, and we will remove access to the work immediately and investigate your claim.



ORIGINAL RESEARCH ARTICLE

Physical oceanographic conditions and a sensitivity study on meltwater runoff in a West Greenland fjord: Kangerlussuaq

Dennis Monteban^{a,b,*}, Jens Olaf Pepke Pedersen^a,
Morten Holtegaard Nielsen^c

^aDTU Space, Technical University of Denmark, Lyngby, Denmark

^bNorwegian University of Science and Technology, Trondheim, Norway

^cMarine Science & Consulting ApS, Copenhagen, Denmark

Received 28 November 2019; accepted 29 June 2020

Available online 11 July 2020

KEYWORDS

Arctic fjord;
Hydrodynamic model;
MIKE 3;
Water masses;
Meltwater runoff;
Kangerlussuaq fjord

Summary In this paper, we discuss the first setup of a hydrodynamic model for the fjord-type estuary Kangerlussuaq, located in West Greenland. Having such a high-fidelity numerical model is important because it allows us to fill in the temporal and spatial gaps left by in situ data and it allows us to examine the response of the fjord to changes in ice sheet runoff. The numerical model is calibrated against in situ data, and a one-year simulation was performed to study the seasonal variability in the physical oceanographic environment and the fjord's response to changing meltwater runoff. The fjord consists of two distinct parts: a deep inner part that is 80 km long with weak currents and a shallow part that covers the outer 100 km of the fjord connected to the ocean. The outer part has very fast currents (~ 1.3 m/s), which we suggest prevents winter sea ice formation. The dominant currents in the fjord are oriented parallel to the long axis of the fjord and are driven by tides and (during summer) freshwater inflow from meltwater-fed rivers. Furthermore, mixing processes are characterized by strong tidal mixing and bathymetric restrictions, and the deep-lying water mass is subject to renewal primarily in wintertime and is almost dynamically decoupled from the open ocean during summertime. Finally, a sensitivity study on the changing meltwater runoff was performed, showing that in-

* Corresponding author at: DTU Space, Technical University of Denmark, Lyngby, Denmark.

E-mail address: dmont@space.dtu.dk (D. Monteban).

Peer review under the responsibility of the Institute of Oceanology of the Polish Academy of Sciences.



Production and hosting by Elsevier

creasing freshwater runoff considerably strengthens stratification in the upper 100 m of the water column in the inner part of the fjord.

© 2020 Institute of Oceanology of the Polish Academy of Sciences. Production and hosting by Elsevier B.V. This is an open access article under the CC BY-NC-ND license (<http://creativecommons.org/licenses/by-nc-nd/4.0/>).

1. Introduction

The largest ice mass in the Northern Hemisphere, the *Greenland Ice Sheet* (GIS), experienced a mass loss of $3,902 \pm 342$ billion tonnes of ice between 1992 and 2018 (Shepherd et al., 2020). The most pronounced effects of climate change, such as the increase in surface air temperature, occur in the Arctic region due to polar amplification (IPCC, 2013), which has increased the freshwater runoff (Trusel et al., 2018). The freshwater discharged from the GIS mostly transits through fjords, where it can be significantly modified before reaching the open ocean (Cottier et al., 2010). Therefore, fjords are considered to be a vital link between the inland ice and the ocean (Straneo and Cenedese, 2015), and it is essential to have a detailed understanding of fjord dynamics. Moreover, an improved understanding of the drivers of fjord circulation is required to explain regional climate changes in Greenland and how the fjord circulation may change in response to changing boundary conditions (Straneo et al., 2013).

Early studies on Arctic fjords were primarily conducted because fjords contain information on past ice sheet variability and sedimentary records (e.g., Storms et al., 2012). Another motivation was that fjord systems contain complex marine ecosystems and because local communities are dependent on fjords for fishing and hunting (e.g., Born and Böcher, 2001). It was relatively recently that the physical oceanographic environment of fjords has been the main focus (Cottier et al., 2010), and such knowledge will allow for a better interpretation of fjord-related research.

The most accurate method to obtain the physical conditions in Arctic fjords is by collecting in situ measurements. However, the harsh Arctic environment, the scale of individual fjords, the number of fjords and the range of time- and space-scales over which important processes occur make it logistically difficult and expensive to collect large amounts of in situ data that are representative of the whole fjord. Therefore, a major limitation in the Arctic is the lack of in situ data. Another approach to obtain an understanding of the physical state of a fjord is modelling. Although numerical models are a simplification of reality, they can act as an additional tool to fill in the spatial and temporal gaps in in situ data and consequently understand the physical processes at work. In addition, numerical models allow one to examine the fjords response to changes in boundary conditions.

A growing body of literature has studied Greenlandic fjord systems (see e.g., Catania et al. (2020) and Rignot et al. (2012) for an overview). These studies have looked at fjords from two different perspectives. The first perspective is that the fjord is a mixing zone where the relevant flow transports heat into the fjord and directly towards the glacier terminus (Cowton et al., 2016; Holland

et al., 2008; Mortensen et al., 2011; Rignot et al., 2010; Sutherland et al., 2014), which affects glacial melting. The other view also regards fjords as mixing zones, but the focus is on the transformation and export of meltwater runoff from the GIS towards the ocean (Straneo et al., 2011), potentially influencing shelf circulation (e.g., Murray et al., 2010).

In this paper, we focus on the fjord Kangerlussuaq (also called Søndre Strømfjord), located in West Greenland. This fjord receives large quantities of freshwater from meltwater-fed rivers each year. Van As et al. (2018) found that the average discharge of the main meltwater river flowing into the fjord, i.e., the Watson River, increased by 46 percent between 2003–2017 compared to the 1949–2002 average. Moreover, the interannual variability in the meltwater runoff increased considerably. However, it is not clear how these variations in meltwater runoff have influenced the fjord Kangerlussuaq. An increase in the annual volume of freshwater runoff from the GIS influences the physical structure of the water column, including the temperature-salinity structure, the strength of the stratification (Kjeldsen et al., 2014; Mortensen et al., 2013) and the primary production (e.g., Arendt et al., 2010; Dziallas et al., 2013). To understand the fjord's response to changing meltwater runoff and the physical oceanographic conditions in general, a hydrodynamic model was established in this study. Additionally, this model is also used to perform a sensitivity analysis by changing the meltwater runoff.

The paper is structured as follows: in Section 2, the study area is described together with the available measurements and observations. Datasets of the freshwater input, the atmospheric parameters and the sea ice cover are used to force the model. In Section 3, the setup of the numerical model is presented, as well as all the model parameters and parameterizations, the model domain and the boundary conditions. We performed a one-year simulation from March 2005 until March 2006 with input data that are a combination of data from multiple years and some are somewhat idealized (meltwater runoff). Therefore, the aim is to determine the seasonal dynamics and the temperature-salinity structure of the fjord as a whole during the period of one year. To gain confidence in the model's performance, we calibrated the model against in situ data of the water level and vertical profiles of the temperature and salinity. This calibration procedure is described in Section 4 and is divided into a barotropic and baroclinic part. The main outputs of the model are presented and discussed in Section 5, which is divided into three parts: 1) the circulation pattern in the fjord, 2) the seasonal dynamics of the water masses and 3) a sensitivity study towards meltwater runoff. Finally, some concluding remarks are presented in Section 6.

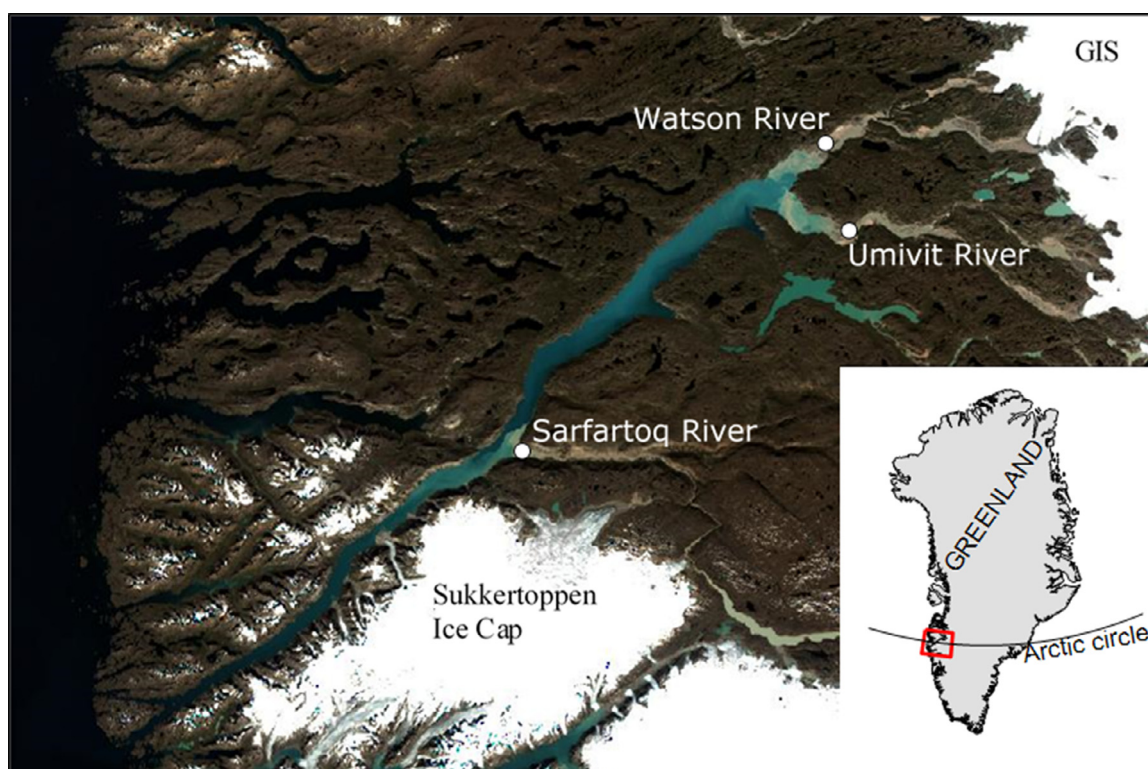


Figure 1 Sentinel-2 true-colour image of the fjord Kangerlussuaq, acquired 31 July 2017. The locations where the three main meltwater rivers enter the fjord are indicated.

2. Study area and observations

2.1. Regional setting

The fjord Kangerlussuaq is a large fjord located at the Arctic circle in West Greenland (Figure 1) and is classified as a fjord-type estuary (Lund-Hansen et al., 2010). The fjord is 180 km long, and there are two branches at the mouth of the fjord that connect the fjord with the open ocean. Further west from the mouth of the fjord at the continental slope, the West Greenland Current is located. The West Greenland Current is a continuation of the East Greenland Current and the Irminger Current, which are governed by the cold and relatively fresh water of Arctic origin and warm and salty water that originated in the Atlantic, respectively (Myers et al., 2007; Sutherland and Pickart, 2008).

In Figure 3, the bathymetry of the fjord Kangerlussuaq, which was surveyed by the Danish Geodata Agency, is presented. The fjord can be divided into two distinct parts: the outer 100 km of the fjord is shallow (30–60 m) and narrow (~1.5 km). The inner part is much deeper (up to 300 m) and wider (~5 km). A steep slope defines the transition between the two parts of the fjord where the bottom rises approximately 215 m over 13 km and is located close to the mouth of the Sarfartoq River (Figure 1).

2.2. Freshwater sources

The fjord receives freshwater from snowmelt, sea-ice melt, precipitation, local glaciers and the GIS. Large quantities of freshwater runoff enter the fjord in the summertime

primarily from three rivers; the Watson River ($66^{\circ}57'54''\text{N}$, $50^{\circ}51'50''\text{W}$) flows into the northeast head of the fjord, the Umivit River ($66^{\circ}50'2''\text{N}$, $50^{\circ}48'37''\text{W}$) enters at the south-east head of the fjord and the Sarfartoq River ($66^{\circ}29'30''\text{N}$, $52^{\circ}1'30''\text{W}$), which enters in approximately the middle of the fjord. The rivers drain meltwater from the GIS and the Sukkertoppen ice cap (Figure 1). Hudson et al. (2014) estimated the catchment area of each river based on the ice surface and basal topography, and this area is 3639 km², 6320 km² and 5385 km² for the Watson River, the Umivit River and the Sarfartoq River, respectively. The catchment area of the Watson River was also determined in multiple previous studies, and this value differs significantly from one study to the other. For instance, catchment areas of 9743 km² (Hasholt et al., 2013), 6130 km² (Mernild et al., 2010), 12547 km² (van As et al., 2012) and 12000 km² (Lindbäck et al., 2015) have been reported. Field measurements of the discharge of the Watson River were conducted by Hasholt et al. (2013) from 2007 to 2010. The peak discharge was usually observed in July/August, and a peak flow of 1620 m³ s⁻¹ was measured. The flow in the rivers is almost zero from October/November until April/May each year, and during 2007–2010, the average annual total discharge volume was 3.7 km³.

2.3. Atmospheric and sea ice observations

Meteorological observations at an elevation of 50 m were obtained from the Danish Meteorological Institute (DMI) weather station, located at the airport of Kangerlussuaq ($67^{\circ}01'\text{N}$, $50^{\circ}42'\text{W}$), which includes the wind speed and

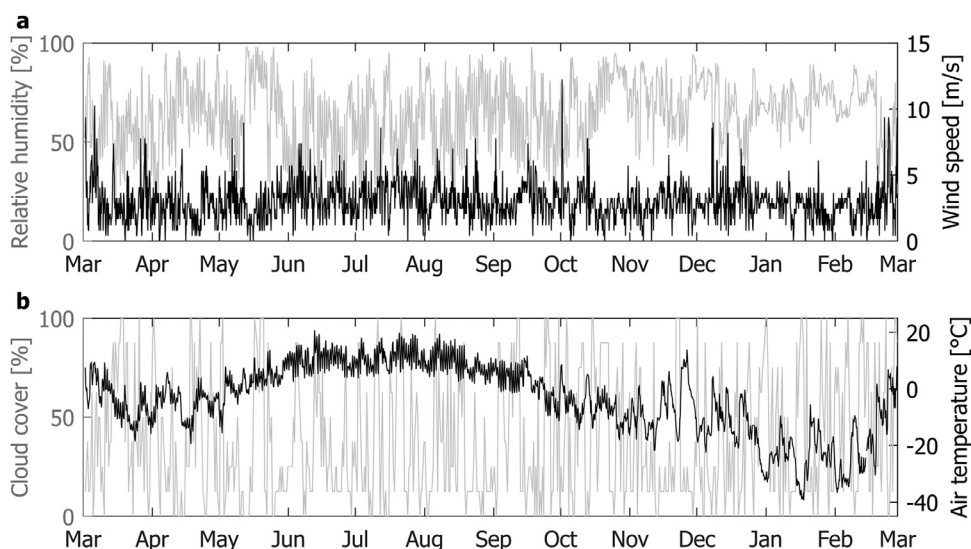


Figure 2 Observations from the DMI weather station, located at the airport of Kangerlussuaq. (a) The relative humidity (gray line) and the wind speed corrected to a height of 10 m above mean sea level (black line). (b) The cloud cover (gray line) and the dry bulb air temperature (black line). The data are taken from Cappelen (2016).

direction, relative humidity, cloud cover and air temperature (Cappelen, 2016). The wind measurements were corrected for height (from 50 m to 10 m above mean sea level) using the wind profile power law (e.g., Shore Protection Manual, 1984). The data were sampled every 1 hour, and the data used to force the model during our one-year simulation are presented in Figure 2 for the period of March 2005 to March 2006.

The mean corrected wind speed for the one-year model simulation is approximately 3 m/s, but some relatively strong winds up to 12.2 m/s were observed. The dominant wind direction is north-easterly, which corresponds to the wind blowing out of the fjord. Typical values for the relative humidity are approximately 70%. The cloud cover varies substantially with cloud-free days (0%) and days with 100% cloud cover. The recorded air temperature varied between approximately +20°C in summer and −38°C in winter. The air temperature dropped below zero degrees around October and was negative until approximately the start of May.

Sea ice formation and breakup were studied using optical imagery collected by the *Moderate-resolution Imaging Spectroradiometer* (MODIS) onboard the Terra and Aqua satellites from the NASA Worldview application during the 2009–2017 period. The sea ice extent is necessary to force the numerical model and for the winter of the one-year model simulation (2005/2006), observations were available from the *Advanced Synthetic Aperture Radar* (ASAR) instrument onboard the Envisat satellite. Generally, initial sea ice formation starts in mid-November, and the fjord is sea ice free beginning in June. Sea ice only forms in the inner part of the fjord and reaches up to approximately 1 metre thick (Hawes et al., 2012; Nielsen et al., 2010). For the winter of 2005/2006, sea ice formation started in the beginning of December 2005 and reached its maximum areal extent at the end of December. The last sea ice floes were observed on 23 May 2006.

2.4. Water level and CTD measurements

Measurements of the water level at several locations throughout the fjord (points a, b and c in Figure 3) were conducted from June 2011 until mid-September 2011 using Solinst Levellogger Gold recording devices (Solinst Canada Ltd, Georgetown, Ontario, Canada). These devices were placed under the waterline during low tide, and they measured the pressure at 5 min intervals. The water levels are computed from the pressure difference as the tidal wave passes, and a mean spring tidal range of 3.5 metres is found. Moreover, the tidal wave travels in approximately 3.5 hours from the open ocean (point a in Figure 3) to the head of the fjord (point c in Figure 3). The tidal character may be defined by the form factor, F , which is the sum of the two main diurnal components (K_1 , O_1) divided by the sum of the two main semidiurnal components (S_2 , M_2) and reads as follows (Courtier, 1939):

$$F = \frac{(K_1 + O_1)}{(M_2 + S_2)}. \quad (1)$$

Classical harmonic analysis using the tidal fitting toolbox (Grindsted, 2020) was used to compute the four tidal constituents in Eq. (1). Based on the form factor, four different types of tides can be distinguished. At the head of the fjord, the form factor has a value of 0.24, which means that the tidal character is classified as semidiurnal.

Conductivity, temperature and pressure data were collected during two surveys that were carried out on 3–5 August 2005 and on 26–27 February 2006. These measurements are described in Nielsen et al. (2010). During the survey in August, a total of 16 vertical profiles were made along the entire fjord using a 19plus SEACAT Profiler (Seabird Electronics, Bellevue, WA, USA). The survey in February includes 6 different vertical profiles that were made on the sea ice-covered part of the fjord; hence, only the inner part of the fjord was surveyed.

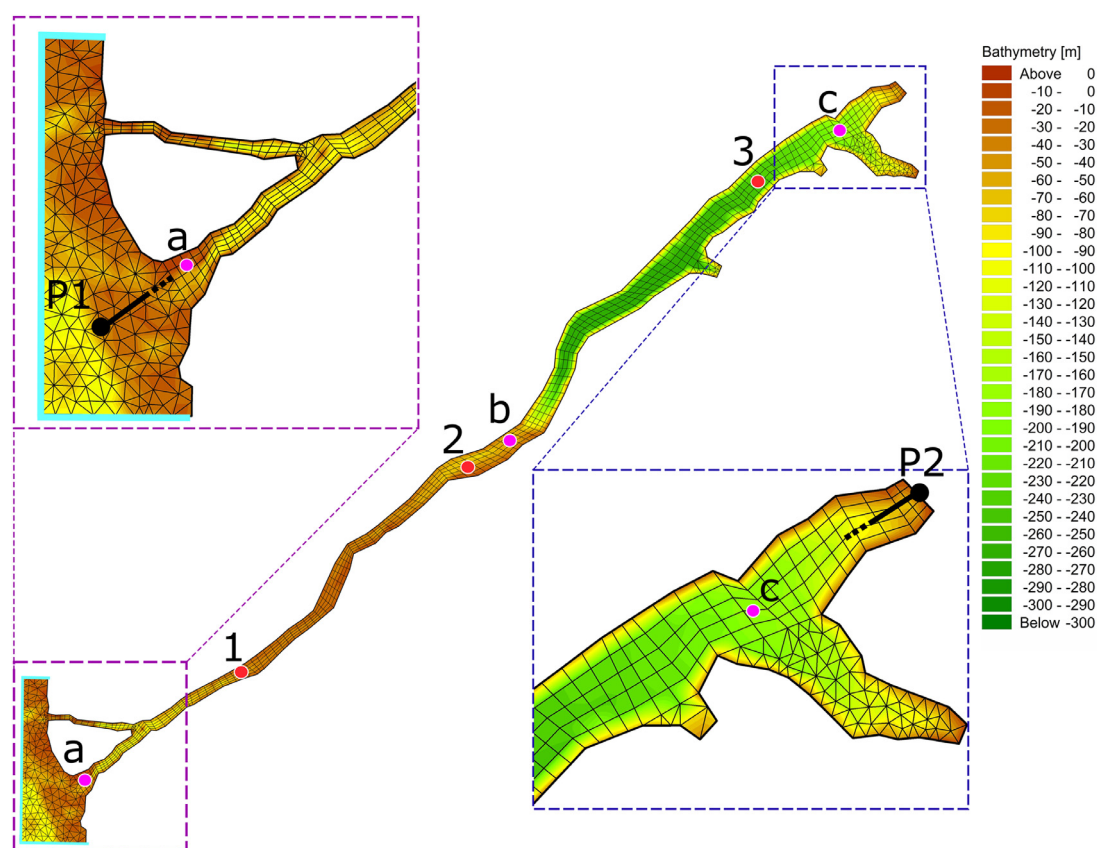


Figure 3 The model domain, bathymetry and horizontal computational mesh. The three red dots (points 1, 2 and 3) indicate the positions of the calibration points for the baroclinic part, and the three magenta dots (points a, b and c) show the calibration points of the barotropic part. The points P1 and P2 shown in the magnifications of the fjord show the beginning and end of the vertical cross sections, which are shown in multiple figures in this paper, respectively. Furthermore, the solid light blue line at the mouth of the fjord depicts the open ocean boundary.

3. Model description

The numerical model of the fjord Kangerlussuaq was implemented using the commercially available three-dimensional MIKE 3 Flow Model (2016 version) software. The MIKE 3 model is well documented, and a comprehensive description can be found in [DHI 2016b](#). An overview of all the input parameters, the choice of the different modules in MIKE 3 and the sources of the boundary and initial conditions used in the simulations are summarized in [Table 1](#). The model setup is described in detail in the remainder of this chapter.

3.1. Model setup

The MIKE 3 model numerically solves the *Reynolds-averaged Navier-Stokes* (RANS) equations with the assumptions of Boussinesq and hydrostatic pressure using a cell-centred finite volume method ([DHI, 2017](#)). The RANS equations are closed with a turbulent scheme by adopting the eddy viscosity concept, where the vertical and horizontal eddy viscosities are represented by the standard $k-\varepsilon$ model ([Rodi, 1984](#)) and the Smagorinsky formulation ([Smagorinsky, 1963](#)), respectively.

The bathymetry of the modelled fjord, the model domain and the horizontal computational mesh are presented in [Figure 3](#). The computational mesh is a combination of triangular elements and quadrangular grid cells. We anticipated a pre-dominant water flow direction along the long axis of the fjord with limited across-fjord variability. Therefore, we used quadrangular grid cells in the main part of the fjord that allow for a coarser resolution in the along-fjord direction than in the across-fjord direction; hence, the number of elements and the computation time are reduced. Moreover, the quadrangular cells simulate the flow more accurately compared to the triangular elements in this case because the elongated quadrangular cells favour water flow along the element, while the triangular elements enhance divergence in the water flow ([DHI, 2016a](#)). The computational mesh has 1984 elements (computational cells) in the surface layer. The smallest element has a characteristic length of approximately 160 m, and the largest cell has a dimension of approximately 1000 m, which is directed along the long axis. The vertical domain was discretized using 40 vertical layers with a resolution of 1 m at the surface layer down to 15 m at the bottom. The first 5 vertical layers starting at the surface are terrain-following sigma layers. The remaining vertical layers are z-layers, which do not follow the bottom terrain and are defined at fixed depths.

Table 1 Overview of the input parameters and module options used in the MIKE 3 model.

Input Parameter	Value or module option
Horizontal mesh	Resolution (min, max) = (160, 1000) m
Vertical mesh	Combined sigma/z-level; 5 sigma layers to a depth of 10 m and 35 z-layers. Resolution (min, max) = (1, 15) m
Time period	1 March 2005–01 March 2006
Maximum time step	300 s
Solution technique	Higher order scheme
Eddy viscosity	Horizontal eddy viscosity: Smagorinsky formulation Vertical eddy viscosity: $k-\varepsilon$ model
Bed resistance	Constant roughness height: 0.05 m
Dispersion	Horizontal dispersion coefficient: 1 Vertical dispersion coefficient: 0.1
Coriolis forcing	Constant in domain
Atmospheric forcing	Observations available from the DMI weather station located at the airport of Kangerlussuaq and includes - Wind speed and direction - Air temperature - Cloud cover - Humidity
Ice coverage	Sea ice coverage derived from Envisat satellite imagery Sea ice roughness: 0.01 m
Initial conditions	Water level 0 m Velocities 0 m s ⁻¹ Salinity from February 2006 measurements (Nielsen et al., 2010) Temperature from February 2006 measurements (Nielsen et al., 2010)
Boundary conditions	Rivers average discharge of 2007–2010 observations (Hasholt et al., 2013) Sea water levels from DTU global tide model Sea salinity and temperature from the Global Ocean Physics Reanalysis product (Copernicus) Sea current velocities from the Global Ocean Physics Reanalysis product (Copernicus)

3.2. Initial and boundary conditions

The initial conditions (simulation started on 01 March 2005) were obtained from the CTD profiles taken on 26 February 2006. Although these measurements are from a different year, we used them because the temperature and salinity distributions throughout the fjord in wintertime are very homogeneous and relatively similar from year to year (Nielsen et al., 2010). The initial conditions in the outer, shallow part of the fjord were obtained by interpolating between the measurements of the vertical profiles in the inner part of the fjord and the values at the open ocean boundary obtained from the E.U. *Copernicus Marine Environment Monitoring Service* (CMEMS) Global Ocean Physics Reanalysis product (CMEMS, 2018). If these initial conditions were not representative of those in the outer part of the fjord, we would expect the model conditions in this region to adjust towards realistic values within a much shorter timescale than the length of the experiment. Since we do not simulate such an adjustment, we argue that this interpolation provides a close approximation to the real conditions within the outer part of the fjord. The lateral boundary condition located outside the mouth of the fjord combines the water level, current velocities, temperature and salinity. Two different sources of data for the open ocean boundary were used. The water level was predicted based on

tidal constituents from the DTU10 global ocean tide model (Cheng and Andersen, 2010). This model includes 10 tidal constituents and has a resolution of $0.125^\circ \times 0.125^\circ$. The output of the DTU10 global ocean tide model compares well with the water level measurements at the mouth of the fjord, with the difference generally being less than 10 cm. The sea water velocities, temperature and salinity were taken from the CMEMS global ocean physics reanalysis product (CMEMS, 2018). This product has a horizontal resolution of $1/12^\circ$, 50 vertical layers down to a depth of 5500 metres and provides daily mean values. The lateral boundary is indicated by the solid light blue line in Figure 3. The barotropic part of the open boundary was specified using Flather's boundary condition (Flather, 1976), which is a combination of the water level and sea water velocities. The water velocities are not necessary to force the model but are imposed for stability reasons. Furthermore, the temperature and salinity were defined as Dirichlet boundary conditions.

The following atmospheric data were included in the model: wind speed and direction, dry bulb air temperature, cloud cover and relative humidity. Observations of these parameters were obtained from the DMI weather station (Figure 2), and these observations are taken as representative values for the entire fjord. The validity of this assumption was checked by comparing the atmospheric data obtained at the Kangerlussuaq airport with those at the

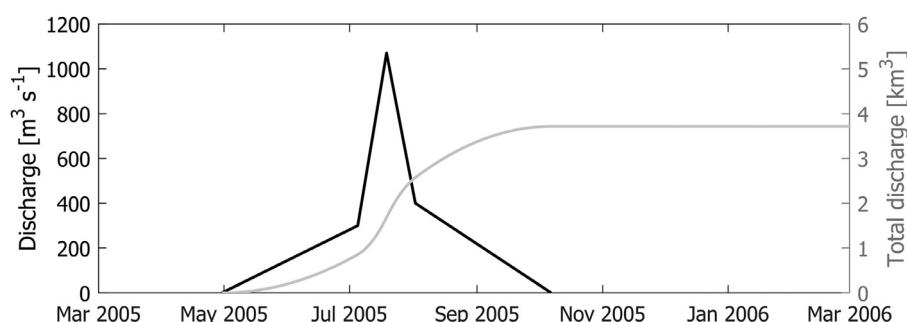


Figure 4 Estimated discharge from the Watson River used as input to the model. The solid black line shows the discharge per second, and the gray solid line shows the accumulated discharge.

Sisimiut airport, which is located further north and closer to the ocean (the comparison is not shown here). Because the inland climate is different from the coastal climate, using values from the Kangerlussuaq airport for the entire fjord may lead to a loss of realism for the atmospheric input data close to the coast. Precipitation and evaporation are neglected because they are assumed to be negligible for our study area. This is because the area of Kangerlussuaq is exceptionally dry due to orographic shielding by the Sukkertoppen ice cap (Box et al., 2006). This dryness, together with water losses from evaporation, causes the contribution of precipitation to be minimal compared to the ice sheet runoff (Hasholt et al., 2013). An input file of the ice concentration was prepared based on Envisat ASAR satellite imagery during November 2005 to May 2006. This file defines the location of the sea ice (ice concentration of 100%) and covers the inner, deep part of the fjord to approximately the Sarfartoq River from December to May.

3.3. Freshwater input

The three meltwater rivers were represented in the model as point sources, which are placed in the surface layer. A ‘simple source’ option was used where the source discharge only contributes to the continuity equation (DHI, 2017). The salinity was set to 0 psu (practical salinity unit) (UNESCO, 1987), and the runoff temperature was set to 1°C. The temperature as well as the discharge of the Watson River has some small-scale fluctuations, where the temperature of the Watson River typically varies between 0°C and 2°C (unpublished data). This is because of the day and night cycle and the resulting changes in air temperature. However, because we are interested in the general circulation pattern in the fjord system, we neglected all the high frequency variations found in the meltwater runoff. Furthermore, we generated an idealised time-series of the discharge, which was based on the average annual discharge of the Watson River during 2007–2010 (Hasholt et al., 2013), see Figure 4. The peak discharge is assumed to occur in late July (Julian day 200) and has a value of 1070 m³ s⁻¹. Based on our idealised time-series of runoff, the average accumulated annual discharge of the Watson River is 3.7 km³. There are no data on the discharges of the Umivit and Sarfartoq Rivers. Therefore, we assumed the same shape as the Watson River discharge (Figure 4), but we scaled the values based on the catchment areas given by Hudson et al. (2014).

Therefore, the discharge of the Watson River is multiplied by factors (6320/3639) and (5385/3639) for the Umivit River and the Sarfartoq River, respectively. The resulting total annual accumulated discharge of the Umivit River is 6.4 km³ and 5.5 km³ for the Sarfartoq River.

4. Model calibration

The model calibration was divided into barotropic and baroclinic parts. It was not possible to perform a validation procedure because of the lack of adequate in situ data.

4.1. Barotropic part

For the barotropic part of the calibration, the simulated surface elevation was calibrated against the water level measurements. However, these measurements (30 July 2011 to 01 September 2011) are not available for our simulated time period (March 2005 to March 2006). Therefore, we performed an additional simulation for the period when the water level measurements were taken. The model setup, sources of the boundary conditions and sources of the atmospheric forcing for the new time period were all the same (Table 1). New input data for the boundary conditions and the atmospheric forcing were generated, but the initial conditions of the salinity and the temperature were kept identical to the 2006 observations. The potential differences in the vertical profiles of salinity and temperature between the simulation periods have a very small influence on the water level variation. This was checked by running the same simulation but with a constant initial temperature of 0°C and salinity of 24 psu. The difference in water level between these simulations was less than 0.02 ± 0.025 m averaged over points a, b and c (see Figure 3).

The resolution of the horizontal computational mesh was the main parameter altered during the calibration of the barotropic part. A sufficiently fine mesh was required to reproduce the observed water levels in the fjord. The influence of the bed roughness was found to be minor and therefore kept as the default value. The model simulation is compared with the observations at points a, b and c in Figure 3. The model simulation is in good agreement with the observations (Figure 5), with a root mean square error of 0.12 m at point c. The phase of the tidal wave is very well reproduced throughout the fjord, meaning we

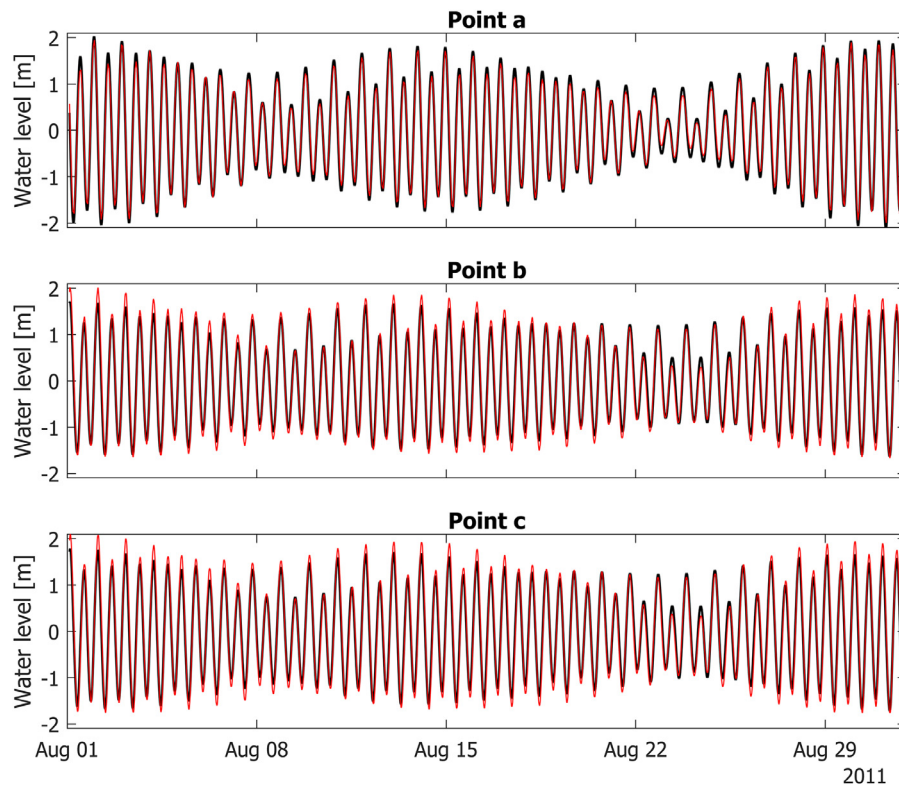


Figure 5 Observed water level (black line) and simulated water level using MIKE 3 (red line) at points a, b and c, as indicated in Figure 3, for a one-month period.

have a good representation of the bathymetry, as this is the main contributor to the phase of the simulated tidal wave. Some discrepancies are present, with a small overestimation during spring tide and an underestimation during neap tide. These minor discrepancies are already observed when comparing the input of the model (from the DTU10 global ocean tide model) at the open ocean boundary with measurements taken outside the fjord (results not shown here). Therefore, the small errors are due to the input of the model at the open ocean boundary, and the model itself reproduces the tides very well.

4.2. Baroclinic part

The second step of the calibration involved comparing vertical profiles of density, salinity and temperature at three points (points 1, 2 and 3 in Figure 3). Two main parameters were altered during this part of the calibration: the type and resolution of the vertical mesh and the vertical dispersion coefficient. Only a few terrain-following sigma layers were adopted because using more of these layers resulted in too much mixing in the deep inner part of the fjord. The reason for this excessive mixing is the very steep slope between the outer and inner parts of the fjord (see Figure 10 around cross section length 100,000 m). If such a steep slope is represented with terrain-following sigma layers, the grid cells are directed almost vertically, which causes significant mixing errors and results in unrealistic flows (DHI, 2016b).

Furthermore, we reduced the vertical dispersion coefficient to a value of 0.1. This low value was required to limit

the amount of vertical mixing, which was found to be too large when using the default value of 1. The necessity of this low dispersion coefficient suggests that there is too much vertical mixing by default in the model.

The comparison between the simulated vertical density, temperature and salinity profiles from the calibrated model and the measurements at the three calibration points is presented in Figure 6. In general, there is a good agreement between the simulation and measurements, which gives us confidence that the main physics are well captured during summertime. A very good comparison is obtained at point 2 and point 3. At point 1, however, deviations are observed in both temperature and salinity. The simulated temperature is approximately 1–2°C warmer than that of the measurements. Moreover, the salinity in the depth range of 10–45 m is too saline. The reason for the deviation in temperature at point 1 is most likely because of the applied boundary condition at the mouth of the fjord. The resolution of the Global Ocean Physics Reanalysis product is much coarser than the vertical resolution of our model, which will lead to some discrepancies. Moreover, we checked the surface temperature of the applied boundary condition (taken from the Global Ocean Physics Reanalysis product) against the measurements made with the Solinst Levelogger recording devices during June–October 2011. The surface temperature taken from the Global Ocean Physics Reanalysis product is generally 0.5–2.5°C warmer than the measurements. This finding strengthens our suspicion that the observed deviations in the temperature at point 1 are due to errors in the applied boundary condition. Overall, the results of the

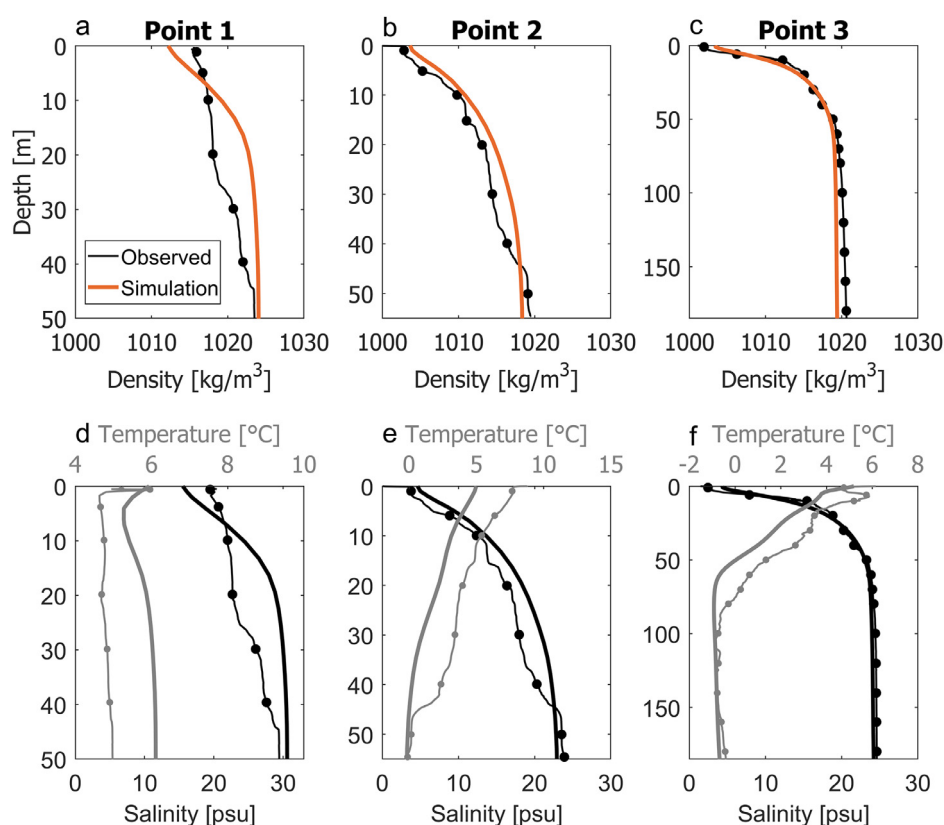


Figure 6 (a–c) Observed (black line with dots) and simulated (solid orange line) vertical profiles of the density at three locations in the fjord, as indicated in Figure 3. (d–f) Observed (line with dots) and simulated (solid line) vertical profiles of the temperature (gray) and salinity (black) at points 1, 2 and 3 for panels (d), (e) and (f), respectively. The profiles were obtained on 3 August 2005.

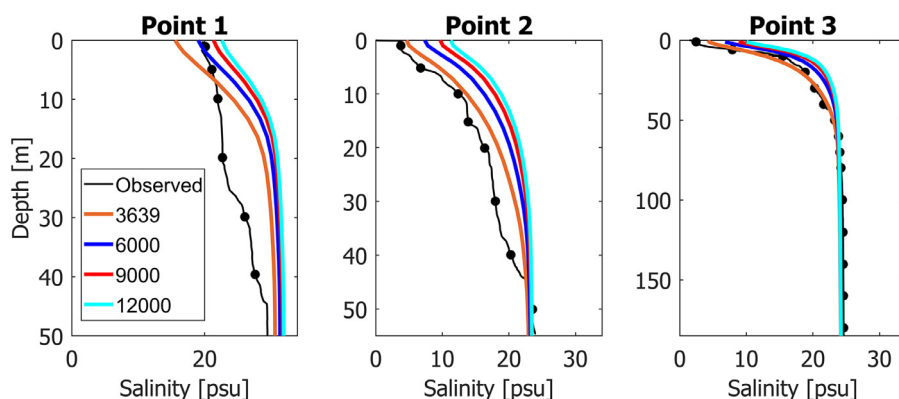


Figure 7 Sensitivity runs of varying meltwater runoff scenarios at points 1, 2 and 3, as indicated in Figure 3. The values given in the legend refer to the catchment area of the Watson River. Note that the value of 3639 km² is the value used in Figure 6. The profiles were obtained on 3 August 2005.

calibration are satisfactory compared with other modelling studies of Arctic fjords such as Young Sound/Tyrolerfjord (Bendtsen et al., 2014) and Hornsund (Jakacki et al., 2017).

4.3. Meltwater forcing sensitivity

As described in Section 2.2, varying Watson River catchment area values were reported in the literature, ranging from 3639 km² to approximately 12000 km². Using a larger

catchment area of the Watson River would reduce the discharges of the Umivit and Sarfartoq Rivers because these values are scaled with the catchment areas. To test the accuracy of the imposed runoff forcing, additional simulations were performed using Watson River catchment areas of 6000 km², 9000 km² and 12000 km². The results of these simulations are presented in Figure 7 for the salinity. The temperature is not shown because the deviation between the different simulations was negligible. From Figure 7, it follows that using a larger catchment area of the Watson

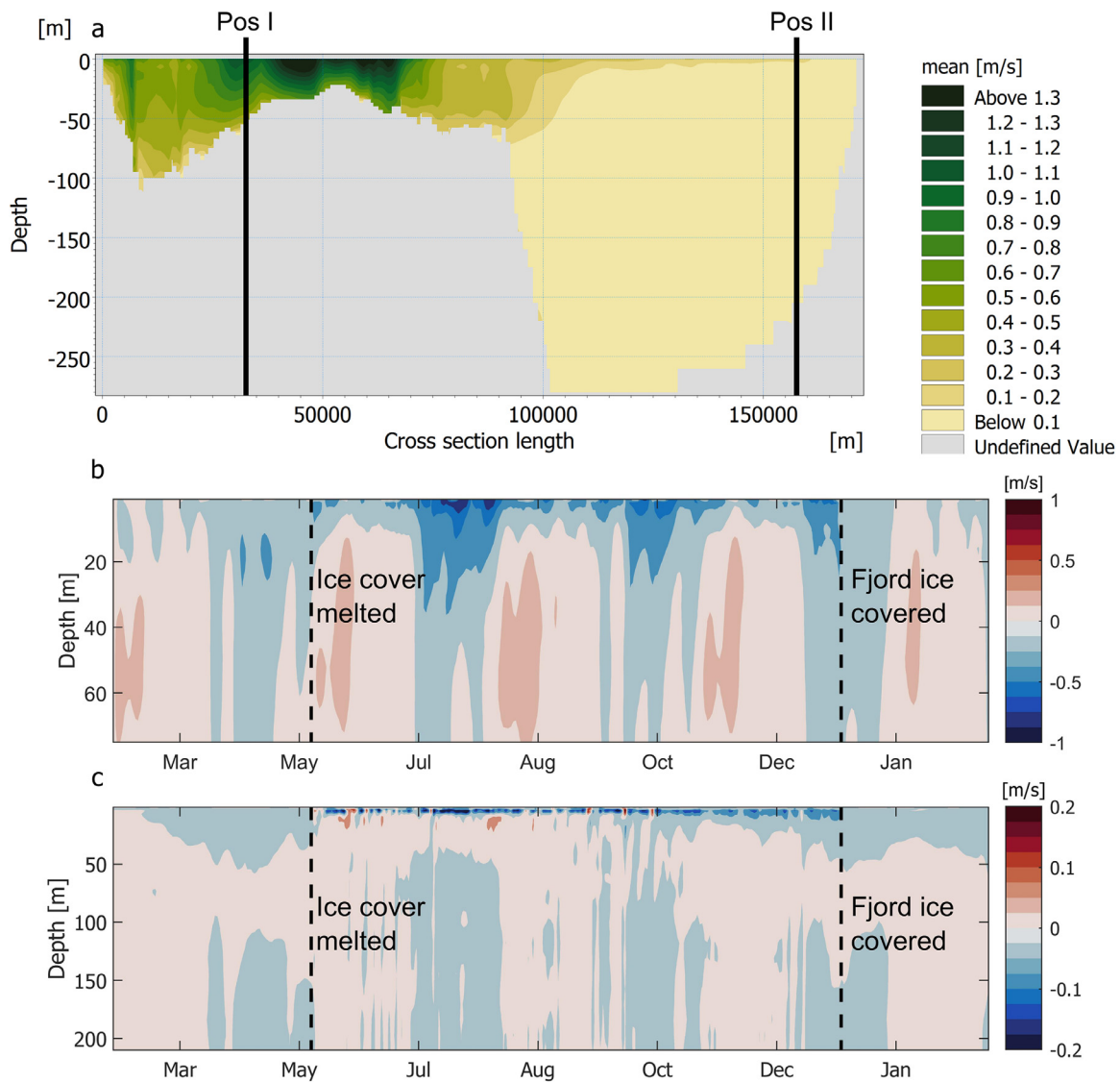


Figure 8 (a) Vertical cross section along the fjord showing the time-averaged, absolute current speed for August 2005. The start and end of the cross section along the fjord are indicated in Figure 3 with points P1 and P2, respectively. Moreover, the vertical transect follows the centreline of the fjord. Lines Pos I and Pos II indicate the locations of the vertical profiles showing the temporal variability in the mean daily currents directed into the fjord from March 2005 until March 2006 in panels (b) and (c), respectively. Note the differences in the definitions of the current speeds in (a) and (b, c); in (a), the shown values are the absolute values, while in (b and c), a positive value indicates a flow directed into the fjord.

River (and therefore a smaller discharge of the Umivit River and Sarfartoq River) results in a salinity that is too high, especially at point 2, which is close to the Sarfartoq River. The best agreement with the measurements is obtained with the used Watson catchment area of 3639 km², giving us confidence in the applied runoff forcing.

5. Results and discussion

5.1. Circulation pattern and currents

The circulation pattern in the fjord is primarily in the along-fjord direction, with currents in the across-fjord direction

being very small. No rotational effects are observed in the fjord, which is supported by computing the internal Rossby radius (e.g., Cottier et al., 2010), which has a value of between 6–12 km at this latitude. The Rossby number is larger than the width of the fjord (approximately 5 km at its widest point), and therefore, rotational dynamics only have a minor influence on the flow. Given that the across-fjord variations are minor, the general circulation in the fjord is studied by plotting the time-averaged current speed along the length of the fjord in Figure 8a for August 2005. The currents in the deep inner part are slow, with typical time-averaged values of approximately 0.05 m/s. In the narrow and shallow middle part of the fjord, averaged values up to 1.3 m/s are observed. Moreover, extremely high instanta-

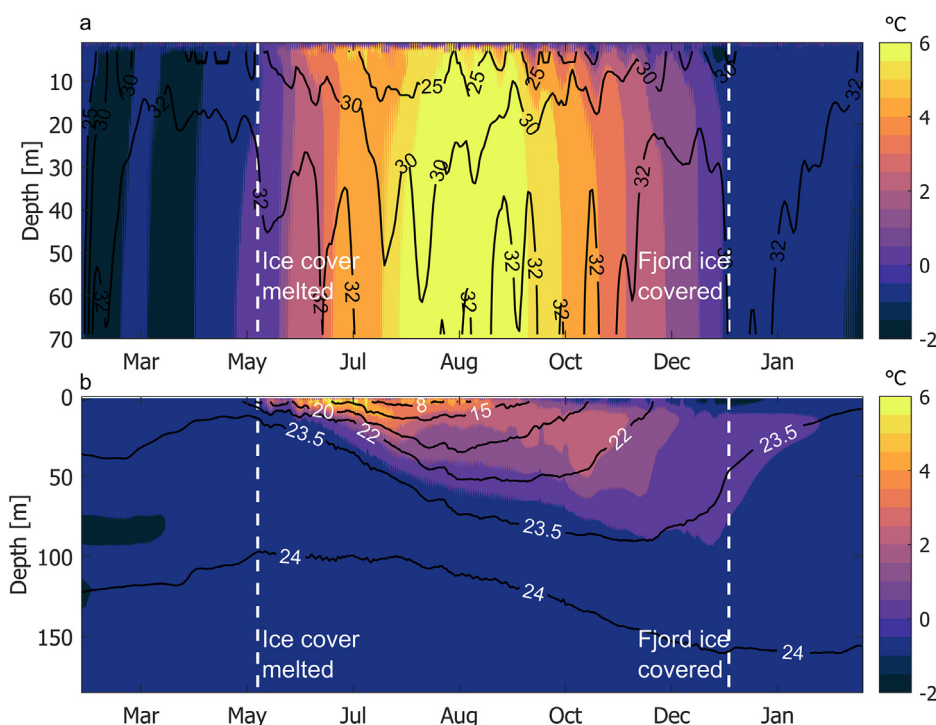


Figure 9 Simulated vertical temperature (colours) and salinity profiles (contour lines) at points 1 (panel a) and 3 (panel b) (see Figure 3) for the one-year simulation (from March 2005 until March 2006).

neous current velocities up to 3.5 m/s were found close to the Sarfartoq River (not shown here), where the width and depth of the fjord are small. The values for the month of August are higher than those in the winter months because in summertime, meltwater inflow from the rivers causes some additional barotropic currents. To show this difference, we plotted the temporal variability in the currents at a location close to the mouth of the fjord in Figure 8b and in the inner, deep part of the fjord in Figure 8c. At both locations, two different regimes are visible. From approximately May until December, there is a net outflow in the upper layer, which is the lower density freshwater-influenced water flowing out. During winter, the discharge from the meltwater rivers is negligible, and no clear vertical gradient in the currents is observed. Furthermore, the spatial variations in modelled current speed (Figure 8a) appear to be related to the spatial variations in sea ice cover in the fjord. Generally, the sea ice cover extends to the middle of the fjord around the mouth of the Sarfartoq River (Figure 1), where the currents are very strong even in winter. Therefore, we suggest that these strong currents prevent the sea ice from forming.

5.2. Seasonal dynamics of water masses

A description of the water masses in the fjord Kangerlussuaq was given by Nielsen et al. (2010), which was based on two surveys of the vertical profiles of salinity and temperature (February 2006 and August 2005) that are used as initial conditions and for the calibration of the model in this paper. By using our numerical model, we provide a more comprehensive image of the seasonal dynamics of the water masses

because we can study the development of the temperature and salinity over a period of one year. The simulated seasonal variation in the vertical salinity and temperature profiles obtained at points 1 and 3 (see Figure 3) are presented in Figure 9. Cross sections of the salinity and temperature along the fjord direction during summer (01 August 2005) and winter (01 March 2006) are shown in Figure 10.

5.2.1. Mixing processes

Understanding how fjord processes modulate mixing between meltwater runoff and coastal waters is vital to understand biological processes such as primary production (Hopwood et al., 2020) and to parametrize fjords in climate models (Straneo and Cenedese, 2015). For the fjord Kangerlussuaq, the salinity and temperature structure indicate that mixing is primarily due to internal processes. The fjord is strongly stratified during summer in the inner part of the fjord. A clear layered structure of the water column is present with the salinity and temperature varying from approximately 5 psu and 7°C at the surface down to 24.5 psu and −0.5°C at the bottom, respectively (Figure 10a and Figure 10b). Wind mixing is only a relatively small contributor to mixing in the fjord because there are gradual changes observed in salinity and temperature in the upper 70 m. A well-mixed, homogeneous top layer would be present if there was strong wind-driven mixing. Therefore, the deep-lying water mass appears shielded from changes in atmospheric conditions on the time-scale of our experiments (Nielsen et al., 2010). This shielding can also be concluded from the fact that the properties of the deep-lying water masses hardly change during summer. The limited wind mixing was also found for the Uummannaq fjord system in

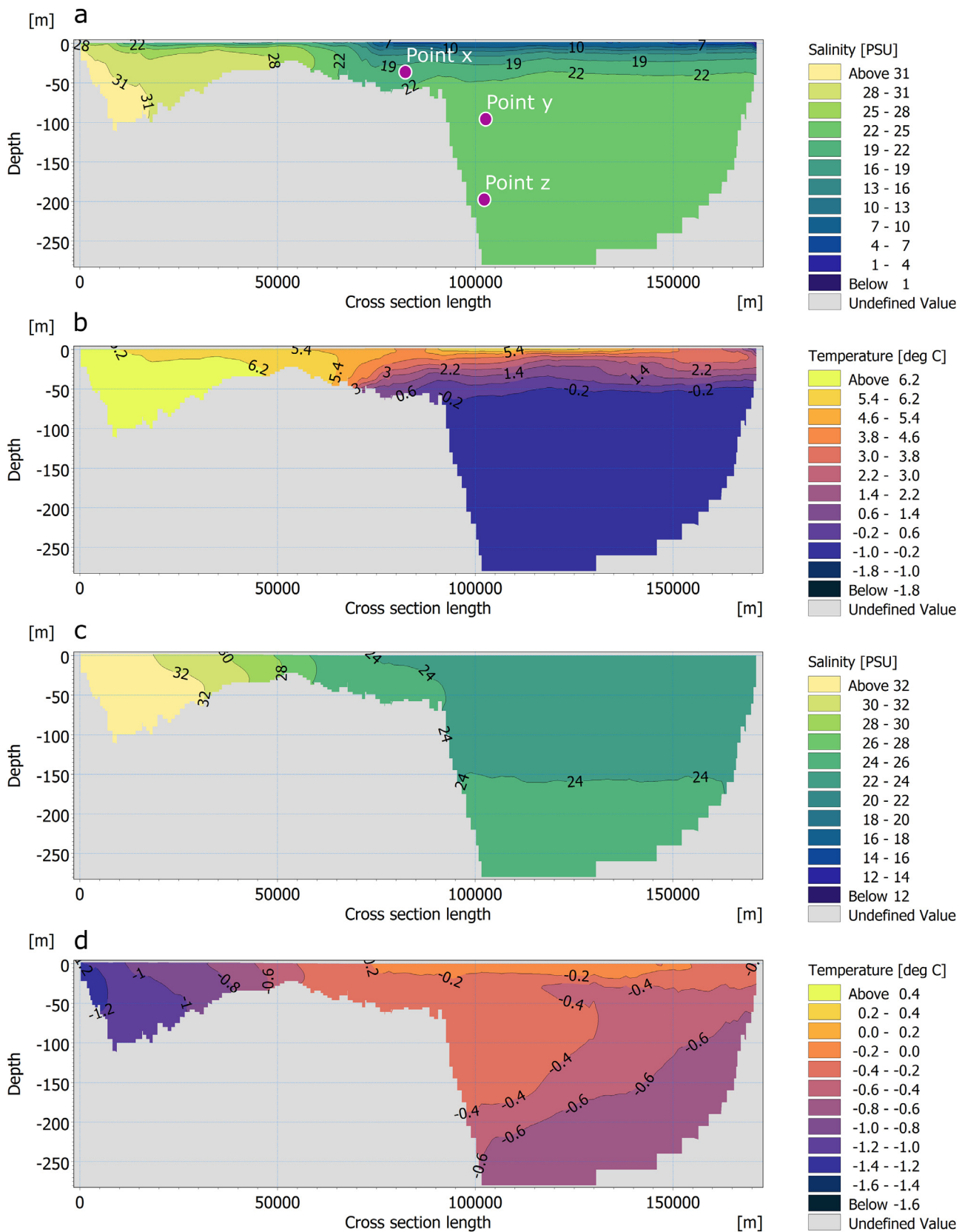


Figure 10 Vertical cross section along the fjord direction of salinity (panels a and c) and temperature (panels b and d) on 01 August 2005 (panels a and b) and 01 March 2006 (panels c and d). The mouth of the fjord is located on the left side of the figure at cross section length 0 m. The start and end of the cross section along the fjord are indicated in Figure 3 with points P1 and P2, respectively. Moreover, the vertical transect follows the centreline of the fjord. Points x, y and z are the locations where the density is extracted in Figure 11.

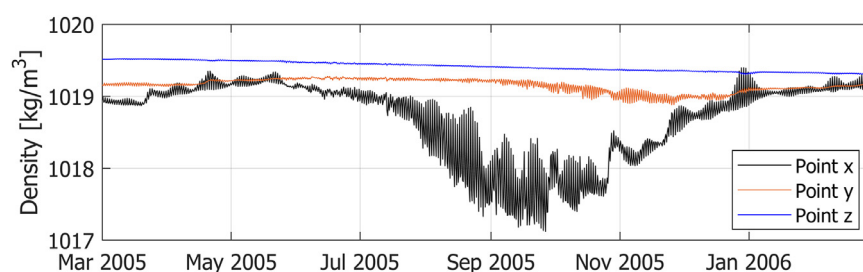


Figure 11 Seasonal density variations at three points (see Figure 10). Point x is located in the shallow inner part of the fjord at a depth of 50 m, and point y and point z are located in the inner, deep part of the fjord at depths of 100 m and 200 m, respectively.

West Greenland (Carroll et al., 2018). Both the Uummannaq fjord and the fjord Kangerlussuaq are therefore exposed to much weaker winds compared to the fjords found in southeast Greenland (Harden and Renfrew, 2012) such as the Sermilik and Kangerdlussuaq fjords (Sutherland et al., 2014). Further, the tidal currents are very fast (~ 1.3 m/s) over the long, shallow sill of the fjord (Figure 8). The strong tidal mixing tends to break down stratification, resulting in a relatively homogeneous water column in the shallow, outer part of the fjord in both winter and summertime (Figure 9a). Therefore, the mixing processes in the fjord Kangerlussuaq are characterized by strong tidal mixing and bathymetric restrictions (the sill).

The fjord Kangerlussuaq shows less stratified conditions in wintertime compared to summertime with salinity values ranging from 23 psu to 24 psu and temperatures from -0.1°C to 0.5°C (Figure 10c and Figure 10d). According to the observations made in February, the temperature should be close to the freezing point throughout the fjord, indicating that sea ice formation and cooling are the dominant physical processes in the winter (Nielsen et al., 2010). The MIKE 3 model is currently unable to include these processes because it does not include a sea ice module. A sea ice cover can be defined, but it is given as external data. When this cover is defined, the atmospheric conditions have no effect on the fjord's surface (sea ice acts as a barrier), and the boundary condition of salinity and temperature in the surface is defined as a Neuman boundary condition that reads as follows:

$$\frac{\partial X}{\partial z} = 0, \quad (2)$$

with X representing either the temperature or salinity, and z is the vertical coordinate. Therefore, the sea ice does not cool the water layers underneath. In addition, freshwater input due to sea ice melt and the process of brine release are not included in the model. These factors are the main drawback of the MIKE 3 model for studying Arctic fjords (Jakacki et al., 2017).

5.2.2. Water masses

Three different water masses are observed in summertime. At the mouth of the fjord, the coastal water is found, which has a salinity of approximately 33 psu and a temperature of 5°C during summer (e.g., Myers et al., 2009). In the inner deep part of the fjord, a runoff-influenced top layer reaching down to approximately 70 m is found lying on top of a deep, relatively cold and saline water mass (Figure 10a and Figure 10b). The top 20 m of this surface layer has

a high temperature of 6°C . Surface insolation may generate such a small warm surface layer during summer, which is observed in many other deep Greenlandic fjords (e.g. Inall et al., 2014; Straneo et al., 2010). The lower part of the runoff-influenced water layer (depth range of 20–70 m) is less dense than the deep-lying water mass but significantly denser than the water found at the surface. From a visual analysis of Figure 9b it follows that this intermediate body of water has a salinity between 15 psu and 23.5 psu and a temperature ranging from 0°C to 4°C . This water was formed between May and August 2005 in our model, when the meltwater runoff was still relatively small (see Figure 9b). The deep-lying water mass has a salinity of approximately 24 psu (Figure 10a) and a temperature of -0.5°C (Figure 10b) and is, therefore, notably different than the water mass found along the coast. This is unusual in comparison with many other Arctic fjords as the coastal water can usually be found in the inner deep basin of the fjord (Carroll et al., 2018; Gladish et al., 2015; Mortensen et al., 2018, 2011). The reason for this is that these fjords have a small sill that allows for a relatively fast exchange between the ocean and the deep-water basin. The fjord Kangerlussuaq, however, has a long shallow sill where the tidal currents are fast, which results in well-mixed conditions causing a dampened exchange between the open ocean and the water mass in the fjord.

5.2.3. Deep-lying water mass

It was suggested by Nielsen et al. (2010) that the dampened exchange between the open ocean and the water mass in the fjord causes the deep-lying water mass to be barely subject to any renewal in summer, which is confirmed by our model results. To check the density of the inflowing water over the sill, we plotted the seasonal variations in density at multiple locations in Figure 11. One point is located in the shallow part of the fjord (directly over the sill) at a depth of 50 m (point x in Figure 10a) and two points in the inner deep part of the fjord at depths of 100 m and 200 m (points y and z in Figure 10a, respectively). All points are close to the steep slope in the bathymetry near the Sarfartoq River (Figure 1). There is barely any change in density at points y and z during the year, while the density at point x shows a variation between summertime and wintertime. This variation is because the incoming water mass of the West Greenland Current at the mouth of the fjord is significantly modified (i.e., mixed with the outflowing freshwater) before reaching the deep inner part of the fjord during summertime. The result is a smaller

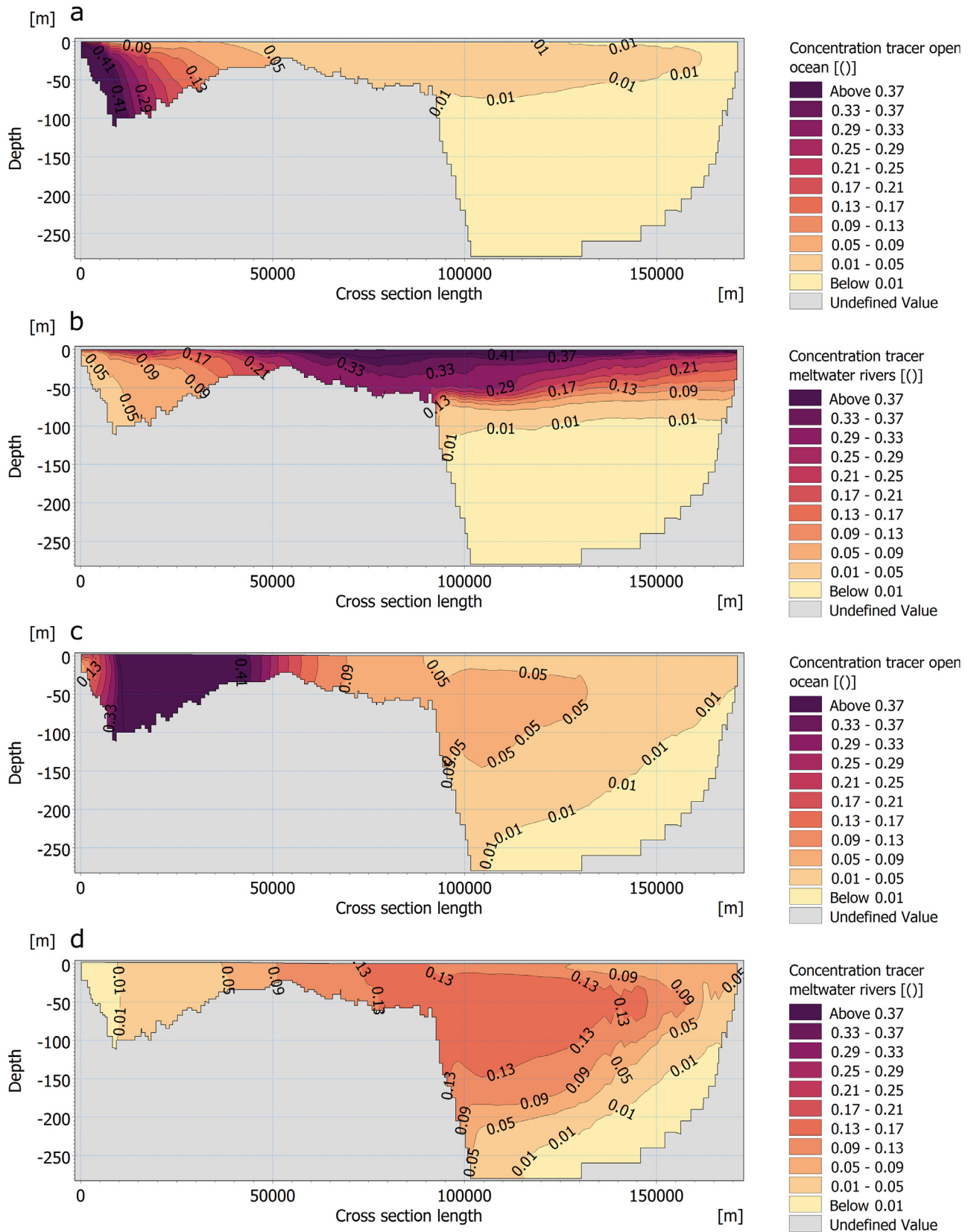


Figure 12 Vertical cross section of the tracer concentration released at the open ocean boundary (a) and (c) and of the tracer concentration released at the meltwater river sources (b) and (d) along the fjord. Subfigures (a) and (b) were obtained on 01 October 2005, (c) and (d) are from 01 March 2006.

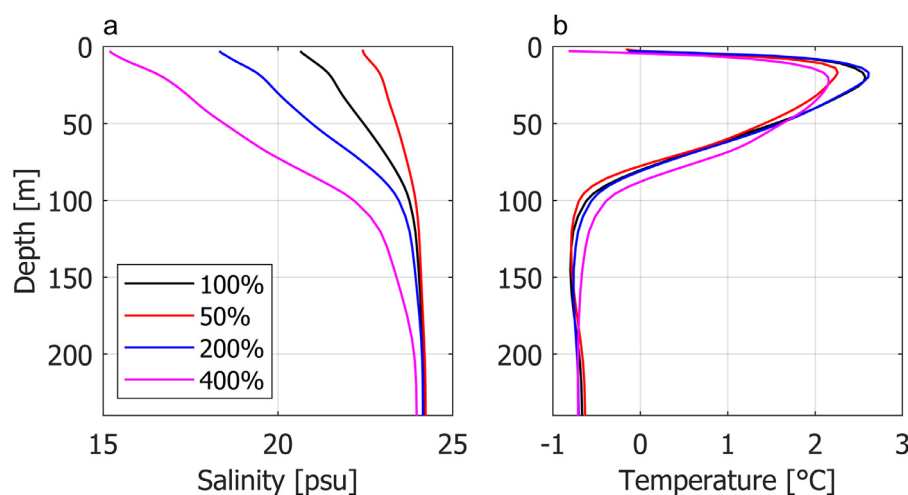


Figure 13 Vertical profiles of the salinity (panel a) and temperature (panel b) at point 3, as given in Figure 3, for the four meltwater runoff scenarios on 01 November 2005.

density at point x than at point y from approximately June to December, which suggests that there is hardly any mixing between these layers during summertime. In addition, the deep part appears to be largely dynamically decoupled from the open ocean during summertime. In other words, changes in temperature and salinity of the coastal water do not propagate into the inner, deep part of the fjord.

To investigate this further, we performed a tracer investigation using the transport module in MIKE 3 (DHI, 2016c). Conservative passive tracers with a concentration of 1 were continuously included, with one tracer at the open ocean boundary and one tracer at the three meltwater river sources. The along-fjord vertical distribution of the tracer's concentration is given in Figure 12. It follows that the deep-lying water mass is hardly influenced by the water mass of the West Greenland Current (Figure 12a) or meltwater runoff (Figure 12b) during the summertime, with tracer concentrations of approximately 0 in the deep part. The deep-lying water mass is (very slowly) renewed by the West Greenland Current water mass (Figure 12c) and meltwater runoff (Figure 12d) during wintertime. Moreover, the meltwater runoff tracer that is present in wintertime (Figure 12d) originated during summertime. This observation is in striking contrast to the typical renewal of deep basin waters, which occurs when the dense coastal water flows over the sill and replaces the deep lying-water mass in fjords (e.g., Carroll et al., 2018; Edwards and Edlsten, 1977; Gladish et al., 2015; Skogseth et al., 2005).

5.3. Meltwater runoff sensitivity analysis

We studied the fjord's response to different meltwater runoff scenarios by running three additional simulations for the March–December period. The total volume of meltwater entering the fjord was either halved, doubled or multiplied by a factor of four compared to the reference case shown in Figure 4, and these cases are referred to as the '50% case', the '200% case' and the '400% case', respectively. In terms of the total annual discharge, the 'base case' has a value of 15.66 km³ (all three meltwater rivers combined). For the 50% case, the total annual discharge is 7.83 km³, the 200%

case has a value of 31.32 km³, and the value for the 400% case is 62.63 km³. For comparison, the maximum observed total annual discharge of the Watson River corresponds to an approximate multiplication of the reference case by a factor of three (van As et al., 2018); therefore, only the 400% case lies outside the range of observations.

The vertical profiles of the temperature and salinity at one location in the fjord are presented in Figure 13. The surface temperature only shows a small deviation among the four scenarios (<0.3°C). In contrast, the different runoff scenarios have a substantial impact on the surface salinity, where it increases by 1.8 psu for the 50% case and reduces by 2.3 psu and 5.5 psu for the 200% and 400% cases, respectively. Similar values are found throughout the inner, deep part of the fjord (not shown here). The stratification in the inner part of the fjord is considerably strengthened with an increase in total meltwater runoff in the upper 100 m of the water column. Furthermore, the deep-lying water mass (below 100 m) only becomes fresher in the 400% case, while it is hardly influenced in the 50% and 200% cases.

It is very likely that the meltwater runoff into the fjord Kangerlussuaq will increase in the future due to climate change, which may have a severe impact on primary production. Lund-Hansen et al. (2018) found that meltwater runoff is the main driver of the variations in optical conditions, inorganic nutrients and primary production during summertime. The increase in meltwater runoff will have two effects on the fjord because the meltwater supplies nutrients and particle matter into the fjord. The increase in nutrient supply will increase productivity, while an increase in particle matter will increase light attenuation, thereby reducing productivity (Murray et al., 2015). However, as Arctic fjords without marine terminating glaciers are generally associated with suppression of primary production (Hopwood et al., 2020), we expect that the net effect of increasing meltwater runoff will reduce primary production in the fjord. This is because stratification impedes the vertical nutrient supply from mixing, and together with light limitation, a reduction of primary production is expected.

6. Conclusions

The commercially available MIKE 3 hydrodynamic model was set up for the fjord Kangerlussuaq to understand its seasonal variability and to study the response to changing freshwater runoff. The model was calibrated against in situ data of the water level and transects of temperature, salinity and density. The main findings are described as follows:

- The general circulation pattern is primarily oriented along the long axis of the fjord, and there is minimal across fjord variations because the fjord is too narrow to be influenced by the Earth's rotational dynamics.
- Two general current regimes are present. The first regime is observed in the summertime, where there are down-fjord currents in the upper 20 m of the water column and up-fjord currents below. The other regime is present during winter, when the freshwater content is negligible and small vertical gradients in the currents are observed.
- The tides are semidiurnal with a mean spring tidal range of 3.5 m.
- The deep inner part of the fjord is characterized by weak currents (~ 0.05 m/s) and is sea ice covered during wintertime. Very fast tidal currents (~ 1.3 m/s) are present in the shallow, outer part of the fjord. We suggest that these fast currents prevent winter sea ice formation in the outer part.
- The mixing processes in the fjord are characterized by strong tidal mixing and bathymetric restrictions.
- The inner part of the fjord is strongly stratified during summer. In the outer part of the fjord, strong tidal mixing tends to breakdown stratification, and smaller vertical gradients in temperature and salinity are observed.
- The deep-lying water mass is hardly subject to any renewal during summertime and is almost dynamically decoupled from the open ocean. The latter is because the water of the West Greenland Current flowing into the fjord over the long shallow sill is heavily modified before reaching the inner part of the fjord, resulting in a density smaller than that of the deep-water mass. This is different compared to many other Arctic fjords, where renewal of deep basin waters occur when dense coastal water flows over the sill and replaces the deep-lying water mass.
- A sensitivity study on meltwater runoff revealed that the surface salinity decreases by approximately 2.3 psu and 5.5 psu when the total discharge flowing into the fjord is doubled or multiplied by a factor of 4, respectively. Moreover, the most severe changes are observed in the upper 100 m in the inner, deep part of the fjord, and shows significant strengthened stratification when the total volume of runoff is increased. Therefore, the predicted increase in meltwater runoff will most likely result in a reduction of primary production.

The main drawback of using the MIKE 3 model to study Arctic fjords is the lack of a sea ice module. Therefore, processes such as cooling, brine release and freshwater release during sea ice melt cannot be included in the model. For the fjord Kangerlussuaq, this means that important physics during wintertime are not captured. For future studies, it is

highly recommended to add a sea ice module to the model, thereby making the model suitable for studying sea ice-covered fjord systems during wintertime. Furthermore, it appears that the model overestimates vertical mixing when the default parameter values are used, and it is highly recommended to investigate this further.

Acknowledgements

We thank and acknowledge DHI for providing access to MIKE 3 and for their assistance implementing the model. We also like to thank Morten Rugbjerg from DHI for his assistance and feedback regarding the model setup. Further, we would like to acknowledge DMI for kindly providing the Envisat data. The Sentinel-2 image used in Figure 1 is available from the ESA and can be downloaded freely from the Sentinel data hub (<https://scihub.copernicus.eu/>). Finally, for the MODIS images used to study the sea ice cover, we acknowledge the use of imagery from the NASA Worldview application (<https://worldview.earthdata.nasa.gov/>), which is part of the NASA Earth Observing System Data and Information System (EOSDIS).

References

- Arendt, K.E., Nielsen, T.G., Rysgaard, S., Tønnesson, K., 2010. Differences in plankton community structure along the Godthåbsfjord, from the Greenland Ice Sheet to offshore waters. *Mar. Ecol. Prog. Ser.* 401, 49–62, <https://doi.org/10.3354/meps08368>.
- Bendtsen, J., Mortensen, J., Rysgaard, S., 2014. Seasonal surface layer dynamics and sensitivity to runoff in a high Arctic fjord (Young Sound/Tyrolerfjord, 74N). *J. Geophys. Res. Ocean.* 119, 2439–2461, <https://doi.org/10.1002/2013JC009622>.
- Born, E.W., Böcher, J., 2001. *The Ecology of Greenland. Atuagkat, Nuuk*, 429 pp.
- Box, J.E., Bromwich, D.H., Veenhuis, B.A., Bai, L.S., Stroeve, J.C., Rogers, J.C., Steffen, K., Haran, T., Wang, S.H., 2006. Greenland ice sheet surface mass balance variability (1988–2004) from calibrated polar MM5 output. *J. Clim.* 19, 2783–2800, <https://doi.org/10.1175/JCLI3738.1>.
- Cappelen, J., 2016. DMI Report 16-08 Weather observations from Greenland – Observation data with description. 1–31.
- Carroll, D., Sutherland, D.A., Curry, B., Nash, J.D., Shroyer, E.L., Catania, G.A., Stearns, L.A., Grist, J.P., Lee, C.M., de Steur, L., 2018. Subannual and Seasonal Variability of Atlantic-Origin Waters in Two Adjacent West Greenland Fjords. *J. Geophys. Res. Ocean.* 123, 6670–6687, <https://doi.org/10.1029/2018JC014278>.
- Catania, G.A., Stearns, L.A., Moon, T.A., Enderlin, E.M., Jackson, R.H., 2020. Future Evolution of Greenland's Marine-Terminating Outlet Glaciers. *J. Geophys. Res. Earth Surf.* 125, 1–28, <https://doi.org/10.1029/2018JF004873>.
- Cheng, Y., Andersen, O.B., 2010. Improvement in global ocean tide model in shallow water regions. *Altimetry for Oceans & Hydrology. OST-ST Meeting, Lisbon*.
- CMEMS, 2018. Global Ocean Physical Reanalysis product. Product Identifier: GLOBAL_REANALYSIS_PHY_001_030. E.U. Copernicus Marine Service Information.
- Cottier, F.R., Nilsen, F., Skogseth, R., Tverberg, V., Skarthamar, J., Svendsen, H., 2010. Arctic fjords: a review of the oceanographic environment and dominant physical processes. *Geol. Soc. London, Spec. Publ.* 344, 35–50, <https://doi.org/10.1144/SP344.4>.

- Courtier, A., 1939. Classification of tides in four types. *Int. Hydrogr. Rev.*
- Cowton, T., Slater, D., Sole, A., Goldberg, D., Nienow, P., 2016. Modeling the impact of glacial runoff on fjord circulation and submarine melt rate using a new subgrid-scale parameterization for glacial plumes. *J. Geophys. Res.-Ocean.* 120, 796–812, <https://doi.org/10.1002/2014JC010324>.
- DHI, 2017. MIKE 3 Flow Model – Scientific Documentation. DHI, Hørsholm, Denmark.
- DHI, 2016a. MIKE zero – Mesh Generator – Step-by-step training guide. DHI, Hørsholm, Denmark.
- DHI, 2016b. MIKE 21 & MIKE 3 Flow Model FM – Hydrodynamic and Transport Module – Scientific Documentation. DHI, Hørsholm, Denmark.
- DHI, 2016c. MIKE 3 FLOW Model FM – Transport Module – User guide. DHI, Hørsholm, Denmark.
- Dziallas, C., Grossart, H.P., Tang, K.W., Nielsen, T.G., 2013. Distinct communities of free-living and copepod-associated microorganisms along a salinity gradient in Godthåbsfjord, West Greenland. *Arctic. Antarct. Alp. Res.* 45, 471–480, <https://doi.org/10.1657/1938-4246.45.4.471>.
- Edwards, A., Edelsten, D.J., 1977. Deep water renewal of Loch Etive: A three basin Scottish fjord. *Estuar. Coast. Mar. Sci.* 5, 575–595, [https://doi.org/10.1016/0302-3524\(77\)90085-8](https://doi.org/10.1016/0302-3524(77)90085-8).
- Flather, R.A., 1976. A tidal model of the north-west European continental shelf. *Mem. Soc. R. Sci. Liege* 10, 141–164.
- Gladish, C.V., Holland, D.M., Rosing-Asvid, A., Behrens, J.W., Boje, J., 2015. Oceanic Boundary Conditions for Jakobshavn Glacier. Part I: Variability and Renewal of Ilulissat Icefjord Waters, 2001–14. *J. Phys. Oceanogr.* 45, 3–32, <https://doi.org/10.1175/JPO-D-14-0044.1>.
- Grindsted, A., 2020. Tidal fitting toolbox Aslak Grindsted (2020). Tidal fitting toolbox. MATLAB Central File Exchange, <https://www.mathworks.com/matlabcentral/fileexchange/19099-tidal-fitting-toolbox> (accessed on May 12, 2020).
- Harden, B.E., Renfrew, I.A., 2012. On the spatial distribution of high winds off southeast Greenland. *Geophys. Res. Lett.* 39, 1–6, <https://doi.org/10.1029/2012GL052245>.
- Hasholt, B., Bech Mikkelsen, A., Holtegaard Nielsen, M., Andreas Dahl Larsen, M., 2013. Observations of Runoff and Sediment and Dissolved Loads from the Greenland Ice Sheet at Kangerlussuaq, West Greenland, 2007 to 2010. *Zeitschrift für Geomorphol.* 57 (Suppl. Iss. 2), 3–27, <https://doi.org/10.1127/0372-8854/2012/S-00121>.
- Hawes, I., Lund-Hansen, L.C., Sorrell, B.K., Nielsen, M.H., Borzák, R., Buss, I., 2012. Photobiology of sea ice algae during initial spring growth in Kangerlussuaq, West Greenland: Insights from imaging variable chlorophyll fluorescence of ice cores. *Photosynth. Res.* 112, 103–115, <https://doi.org/10.1007/s11120-012-9736-7>.
- Holland, D.M., Thomas, R.H., De Young, B., Ribergaard, M.H., Lyberth, B., 2008. Acceleration of Jakobshavn Isbr triggered by warm subsurface ocean waters. *Nat. Geosci.* 1, 659–664, <https://doi.org/10.1038/ngeo316>.
- Hopwood, M.J., Carroll, D., Dunse, T., Hodson, A., Holding, J.M., Iriarte, J.L., Ribeiro, S., Achterberg, E.P., Cantoni, C., Carlson, D.F., Chierici, M., Clarke, J.S., Cozzi, S., Fransson, A., Juul-Pedersen, T., Winding, M.H.S., Meire, L., 2020. Review article: How does glacier discharge affect marine biogeochemistry and primary production in the Arctic? *Cryosphere* 14, 1347–1383, <https://doi.org/10.5194/tc-14-1347-2020>.
- Hudson, B., Overeem, I., McGrath, D., Syvitski, J.P.M., Mikkelsen, A., Hasholt, B., 2014. MODIS observed increase in duration and spatial extent of sediment plumes in Greenland fjords. *Cryosphere* 8, 1161–1176, <https://doi.org/10.5194/tc-8-1161-2014>.
- Inall, M.E., Murray, T., Cottier, F.R., Scharrer, K., Boyd, T.J., Heywood, K.J., Bevan, S.L., 2014. Oceanic heat delivery via Kangerdlugssuaq Fjord to the south-east Greenland ice sheet. *J. Geophys. Res.-Oceans*, 119, 631–645, <https://doi.org/10.1002/2013JC009295>.
- IPCC, 2013. Climate Change 2013: The Physical Science Basis. Contribution of Working Group I to the Fifth Assessment Report of the Intergovernmental Panel on Climate Change. Cambridge Univ. Press, Cambridge, UK, New York, USA, 1535 pp.
- Jakacki, J., Przyborska, A., Kosecki, S., Sundfjord, A., Albrechtsen, J., 2017. Modelling of the Svalbard fjord Hornsund. *Oceanologia* 59 (4), 473–495, <https://doi.org/10.1016/j.oceano.2017.04.004>.
- Kjeldsen, K.K., Mortensen, J., Bendtsen, J., Petersen, D., Lennert, K., Rysgaard, S., 2014. Ice-dammed lake drainage cools and raises surface salinities in a tidewater outlet glacier fjord, west Greenland. *J. Geophys. Res.* 119 (6), 1310–1321, <https://doi.org/10.1002/2013JF003034>.
- Lindbäck, K., Pettersson, R., Hubbard, A.L., Doyle, S.H., Van As, D., Mikkelsen, A.B., Fitzpatrick, A.A., 2015. Subglacial water drainage, storage, and piracy beneath the Greenland ice sheet. *Geophys. Res. Lett.* 42, 7606–7614, <https://doi.org/10.1002/2015GL065393>.
- Lund-Hansen, L.C., Andersen, T.J., Nielsen, M.H., Pejrup, M., 2010. Suspended Matter, Chl-*a*, CDOM, Grain Sizes, and Optical Properties in the Arctic Fjord-Type Estuary, Kangerlussuaq, West Greenland During Summer. *Estuar. Coast.* 33, 1442–1451, <https://doi.org/10.1007/s12237-010-9300-7>.
- Lund-Hansen, L.C., Hawes, I., Holtegaard Nielsen, M., Dahllöf, I., Sorrell, B.K., 2018. Summer meltwater and spring sea ice primary production, light climate and nutrients in an Arctic estuary, Kangerlussuaq, west Greenland. *Arctic Antarct. Alp. Res.* 50, art. no. e1414468, 11 pp., <https://doi.org/10.1080/15230430.2017.1414468>.
- Mernild, S.H., Liston, G.E., Steffen, K., Van Den Broeke, M., Hasholt, B., 2010. Runoff and mass-balance simulations from the Greenland Ice Sheet at Kangerlussuaq (Søndre Strømfjord) in a 30-year perspective, 1979–2008. *Cryosphere* 4, 231–242, <https://doi.org/10.5194/tc-4-231-2010>.
- Mortensen, J., Bendtsen, J., Motyka, R.J., Lennert, K., Truffer, M., Fahnestock, M., Rysgaard, S., 2013. On the seasonal freshwater stratification in the proximity of fast-flowing tidewater outlet glaciers in a sub-Arctic sill fjord. *J. Geophys. Res.-Oceans* 118, 1382–1395, <https://doi.org/10.1002/jgrc.20134>.
- Mortensen, J., Lennert, K., Bendtsen, J., Rysgaard, S., 2011. Heat sources for glacial melt in a sub-Arctic fjord (Godthåbsfjord) in contact with the Greenland Ice Sheet. *J. Geophys. Res.-Oceans* 116, (C1), art. no. C01013, 13 pp., <https://doi.org/10.1029/2010JC006528>.
- Mortensen, J., Rysgaard, S., Arendt, K.E., Juul-Pedersen, T., Søgaard, D.H., Bendtsen, J., Meire, L., 2018. Local Coastal Water Masses Control Heat Levels in a West Greenland Tidewater Outlet Glacier Fjord. *J. Geophys. Res.-Oceans* 123, 8068–8083, <https://doi.org/10.1029/2018JC014549>.
- Murray, C., Markager, S., Stedmon, C.A., Juul-Pedersen, T., Sejrh, M.K., Bruhn, A., 2015. The influence of glacial melt water on bio-optical properties in two contrasting Greenlandic fjords. *Estuar. Coast. Shelf Sci.* 163, 72–83, <https://doi.org/10.1016/j.ecss.2015.05.041>.
- Murray, T., Scharrer, K., James, T.D., Dye, S.R., Hanna, E., Booth, A.D., Selmes, N., Luckman, A., Hughes, A.L.C., Cook, S., Huybrechts, P., 2010. Ocean regulation hypothesis for glacier dynamics in southeast Greenland and implications for ice sheet mass changes. *J. Geophys. Res.* 115, 1–15, <https://doi.org/10.1029/2009JF001522>.
- Myers, P.G., Donnelly, C., Ribergaard, M.H., 2009. Structure and variability of the West Greenland Current in Summer derived from 6 repeat standard sections. *Prog. Oceanogr.* 80, 93–112, <https://doi.org/10.1016/j.jocean.2008.12.003>.
- Myers, P.G., Kulan, N., Ribergaard, M.H., 2007. Irminger water vari-

- ability in the West Greenland Current. *Geophys. Res. Lett.* 34, 2–7, <https://doi.org/10.1029/2007GL030419>.
- Nielsen, M.H., Erbs-Hansen, D.R., Knudsen, K.L., 2010. Water masses in Kangerlussuaq, a large fjord in West Greenland: the processes of formation and the associated foraminiferal fauna. *Polar Res.* 29, 159–175, <https://doi.org/10.1111/j.1751-8369.2010.00147.x>.
- Rignot, E., Fenty, I., Menemenlis, D., Xu, Y., 2012. Spreading of warm ocean waters around Greenland as a possible cause for glacier acceleration. *Ann. Glaciol.* 53, 257–266, <https://doi.org/10.3189/2012AoG60A136>.
- Rignot, E., Koppes, M., Velicogna, I., 2010. Rapid submarine melting of the calving faces of West Greenland glaciers. *Nat. Geosci.* 3, 187–191, <https://doi.org/10.1038/ngeo765>.
- Rodi, W., 1984. Turbulence models and their application in hydraulics. *Internat. Assoc. Hydraulic Res. Delft*.
- Shepherd, A., Ivins, E., Rignot, E., Smith, B., van den Broeke, M., Velicogna, I., Whitehouse, P., Briggs, K., Joughin, I., Krinner, G., Nowicki, S., Payne, T., Scambos, T., Schlegel, N., A. G., Agosta, C., Ahlstrøm, A., Babonis, G., Barletta, V.R., Bjørk, A.A., Blazquez, A., Bonin, J., Colgan, W., Csatho, B., Cullather, R., Engdahl, M.E., Felikson, D., Fettweis, X., Forsberg, R., Hogg, A.E., Gallee, H., Gardner, A., Gilbert, L., Gourmelen, N., Groh, A., Gunter, B., Hanna, E., Harig, C., Helm, V., Horvath, A., Horwath, M., Khan, S., Kjeldsen, K.K., Konrad, H., Langen, P.L., Lecavalier, B., Loomis, B., Luthcke, S., McMillan, M., Melini, D., Mernild, S., Mohajerani, Y., Moore, P., Mottram, R., Mougnot, J., Moyano, G., Muir, A., Nagler, T., Nield, G., Nilsson, J., Noël, B., Otsuka, I., Pattie, M.E., Peltier, W.R., Pie, N., Rietbroek, R., Rott, H., Sandberg Sørensen, L., Sasgen, I., Save, H., Scheuchl, B., Schrama, E., Schröder, L., Seo, K.W., Simonsen, S.B., Slater, T., Spada, G., Sutterley, T., Talpe, M., Tarasov, L., van de Berg, W.J., van der Wal, W., van Wessel, M., Vishwakarma, B.D., Wiese, D., Wilton, D., Wagner, T., Wouters, B., Wuite, J., 2020. Mass balance of the Greenland Ice Sheet from 1992 to 2018. *Nature* 579, 233–239, <https://doi.org/10.1038/s41586-019-1855-2>.
- Shore Protection Manual, 1984. *Shore Protection Manual. US Army Corps of Engineers, Washington DC*.
- Skogseth, R., Haugan, P.M., Jakobsson, M., 2005. Watermass transformations in Storfjorden. *Cont. Shelf Res.* 25, 667–695, <https://doi.org/10.1016/j.csr.2004.10.005>.
- Smagorinsky, J., 1963. General Circulation Experiments With the Primitive Equations. *Mon. Weather Rev.* 91, 99–164, [https://doi.org/10.1175/1520-0493\(1963\)091<0099:gcewtp>2.3.co;2](https://doi.org/10.1175/1520-0493(1963)091<0099:gcewtp>2.3.co;2).
- Storms, J.E.A., de Winter, I.L., Overeem, I., Drijkoningen, G.G., Lykke-Andersen, H., 2012. The Holocene sedimentary history of the Kangerlussuaq Fjord-valley fill, West Greenland. *Quat. Sci. Rev.* 35, 29–50, <https://doi.org/10.1016/j.quascirev.2011.12.014>.
- Straneo, F., Cenedese, C., 2015. The Dynamics of Greenland's Glacial Fjords and Their Role in Climate. *Ann. Rev. Mar. Sci.* 7, 89–112, <https://doi.org/10.1146/annurev-marine-010213-135133>.
- Straneo, F., Curry, R.G., Sutherland, D.A., Hamilton, G.S., Cenedese, C., Våge, K., Stearns, L.A., 2011. Impact of fjord dynamics and glacial runoff on the circulation near Helheim Glacier. *Nat. Geosci.* 4, 322–327, <https://doi.org/10.1038/ngeo1109>.
- Straneo, F., Hamilton, G.S., Sutherland, D.A., Stearns, L.A., Davidson, F., Hammill, M.O., Stenson, G.B., Rosing-Asvid, A., 2010. Rapid circulation of warm subtropical waters in a major glacial fjord in East Greenland. *Nat. Geosci.* 3, 182–186, <https://doi.org/10.1038/ngeo764>.
- Straneo, F., Heimbach, P., Sergienko, O., Hamilton, G., Catania, G., Griffies, S., Hallberg, R., Jenkins, A., Joughin, I., Motyka, R., Pfeffer, W.T., Price, S.F., Rignot, E., Scambos, T., Truffer, M., Vieli, A., 2013. Challenges to Understand the Dynamic Response of Greenland's Marine Terminating Glaciers to Oceanic and Atmospheric Forcing. *Bull. Am. Meteorol. Soc.* 94 (8), 1131–1144, <https://doi.org/10.1175/BAMS-D-12-00100.1>.
- Sutherland, D.A., Pickart, R.S., 2008. The East Greenland Coastal Current: Structure, variability, and forcing. *Prog. Oceanogr.* 78, 58–77, <https://doi.org/10.1016/j.poccean.2007.09.006>.
- Sutherland, D.A., Straneo, F., Pickart, R.S., 2014. Characteristics and dynamics of two major Greenland glacial fjords. *J. Geophys. Res.-Oceans* 119, 3767–3791, <https://doi.org/10.1002/2013JC009786>.
- Trusel, L.D., Das, S.B., Osman, M.B., Evans, M.J., Smith, B.E., Fettweis, X., McConnell, J.R., Noël, B.P.Y., van den Broeke, M.R., 2018. Nonlinear rise in Greenland runoff in response to post-industrial Arctic warming. *Nature* 564, 104–108, <https://doi.org/10.1038/s41586-018-0752-4>.
- UNESCO, 1987. *International oceanographic tables. Unesco Tech. Pap. Mar. Sci.* 3, 195 pp.
- van As, D., Hasholt, B., Ahlstrøm, A.P., Box, J.E., Cappelen, J., Colgan, W., Fausto, R.S., Mernild, S.H., Mikkelsen, A.B., Noël, B.P.Y., Petersen, D., van den Broeke, M.R., 2018. Reconstructing Greenland Ice Sheet meltwater discharge through the Watson River (1949–2017). *Arctic, Antarct. Alp. Res.* 50 (1), art. no. e1433799, 10 pp., <https://doi.org/10.1080/15230430.2018.1433799>.
- van As, D., Hubbard, A.L., Hasholt, B., Mikkelsen, A.B., van den Broeke, M.R., Fausto, R.S., 2012. Large surface meltwater discharge from the Kangerlussuaq sector of the Greenland ice sheet during the record-warm year 2010 explained by detailed energy balance observations. *Cryosphere* 6, 199–209, <https://doi.org/10.5194/tc-6-199-2012>.